Hindawi
International Journal of Energy Research
Volume 2023, Article ID 1524859, 18 pages
https://doi.org/10.1155/2023/1524859

Research Article

Facile Solvothermal Synthesis of NiO/g-C_3N_4 Nanocomposite for Enhanced Supercapacitor Application

Shri Hari S. Pai,[1] **Ananta Sasmal**,[1] **Arpan Kumar Nayak**,[1,2] **and HyukSu Han**[2]

[1]*Department of Physics, School of Advanced Sciences, Vellore Institute of Technology, Vellore, 632014 Tamil Nadu, India*
[2]*Department of Energy Engineering, Konkuk University, 120 Neungdong-ro, Seoul 05029, Republic of Korea*

Correspondence should be addressed to Arpan Kumar Nayak; aknayakju@gmail.com and HyukSu Han; hhan@konkuk.ac.kr

Received 7 February 2023; Revised 3 May 2023; Accepted 6 May 2023; Published 22 May 2023

Academic Editor: Thangjam Ibomcha Singh

There is a desperate demand for efficient energy storage systems to fulfill future energy demands. Herein, we exemplify a facile solvothermal approach followed by heat treatment to synthesize NiO/g-C_3N_4 nanocomposites for enhanced supercapacitor applications. The molar ratio of g-C_3N_4 is varied to achieve numerous nanostructures like nanoparticles and nanorods with optimum specific capacitance. Further, all as-prepared electrode materials are examined for supercapacitor application. The electrochemical behavior of prepared NiO/g-C_3N_4 nanocomposites is carried out under cyclic voltammetry (CV), galvanostatic charge-discharge (GCD), and electrochemical impedance spectroscopy (EIS) in a three-electrode cell under different electrolytes such as aqueous sodium sulphate electrolyte (1.0 M Na_2SO_4) and potassium hydroxide electrolyte (3.0 M KOH). Among all the electrode materials, NO-4 (1 : 2) shows the highest specific capacitance of 338.68 F/g at a scan rate of 2 mV/s and 161.3 F/g at a current density of 1 A/g in 1.0 M Na_2SO_4 electrolyte. Also, this electrode material shows 95.22 F/g at a scan rate of 2 mV/s in 3.0 M KOH electrolyte. The excessive specific capacitance of this electrode material is due to retarded charge transfer resistance in the interface at the electrode and electrolyte and a increased number of active sites. The investigation of the electrokinetics of all the prepared electrodes was also carried out, and it revealed the charge storage contribution of capacitive and diffusive parts which levitates the higher specific capacitance. The two-electrode study for evaluating supercapacitor performance is studied. The NO-4//NO-4 SSD in 1.0 M Na_2SO_4 electrolyte shows 18.23 F/g at a specific capacitance of 1 A/g with a corresponding energy density of 10.13 Wh/kg and a power density of 1.01 kW/kg, respectively.

1. Introduction

Owing to the diminution of fossil fuels due to the rapid growth of the world population and economy, we need sustainable and persistent energy sources [1]. Renewable energy production, namely, solar energy [2], wind energy [3], ocean wave energy, tidal energy [4], and biogas [5], caught the interest of scientists to generate energy. Bottlenecks in these renewable sources are intermittent and highly discontinuous; hence, there is a need for energy storage for future generation. In fact, tremendous endeavors have been achieved for the elevated performance of energy storage devices, in that supercapacitors (SCs) have gained attention due to their excellent electrochemical performance, high power density, ultrafast charge and discharge, long stability, eco-friendliness, and a wide band of applications in electronic and hybrid transport facilities [6–11]. Based on the charge storage mechanism, SCs can be branched into two types, and they are electric double-layer capacitors (EDLCs) and pseudocapacitors [12]. The EDLC uses a mechanism of adsorption of ions and stores charge electrostatically whereas the mechanism of rapidly reversible redox reactions on the surface of the electrodes is used in pseudocapacitors [13–15]. Pseudocapacitor's redox process significantly produces more dominant specific capacitance and performances than the EDLCs [16]. The operation of the SCs depends on the electrode materials which should possess merits such as flexibility, tolerance of chemical and various physical environments, ecological benignity, and economical [17]. In this perspective, transition metal oxides (TMOs) are a befitting contender for pseudocapacitive electrode material due to their excellent and rich redox chemistry

[18]. The outstanding TMO candidates are NiO [19], CeO_2 [20], Fe_2O_3 [21], MnO_2 [22], In_2O_3 [23], CuO [24], ZnO [25], etc. Among the above mentioned TMOs, nickel oxide electrode materials stand out as one of the promising candidate because of its better electrical conductivity, good thermal stability, low cost, and nature friendly character [26–29]. Nickel oxide shows excellent pseudocapacitive behavior due to its eminent insertion and extraction of the electrolyte ions and has a high theoretical capacitance value [30]. The highly porous nature and surface area nature favor the diffusion process and enhance the transportation of the electrons in the electrode materials which can be witnessed in nickel oxides [31, 32]. Further incorporation of nickel oxide and nickel hydroxide in various TMOs enhanced the specific capacitance of the electrodes due to sufficient increment in surface active sites and electrical conductivity [33, 34]. Various NiO nanostructures such as NiO nanoparticles (specific capacitance of 74 F/g at 1 A/g in 1.0 M Na_2SO_4 neutral electrolyte and specific capacitance of 116 F/g at 1 A/g in 1.0 M KOH basic solution) [35], NiO nanoflakes (specific capacitance of 85.5 F/g at 1 A/g in 2.0 M KOH basic electrolyte) [36], and NiO nanocrystal (specific capacitance of 85 F/g at 1 A/g in 0.5 M KOH basic solution) [37] exhibited encouragement for applications of SCs. It should be noted that the performance in terms of the capacitance of the nickel oxide nanoparticles is significantly low in neutral media. Thus, it is important to develop NiO-based nanocomposites to enhance the capacitive behavior by increasing active sites, electrical conductivity, and the interaction between the electrode and electrolyte interface [38, 39]. In this context, Gao et al. showed NiO/RGO nanocomposite with a specific capacitance of 68.9 mAh/g at 1 A/g in a 6.0 M KOH electrolyte [40]. Ashok et al. recently disclosed coincorporated NiO nanomaterial which exhibits a specific capacitance of 156 C/g at 0.5 A/g in 3.0 M KOH electrolyte [41]. CNT/ZnO/NiO nanocomposites prepared by Jayababu et al. exhibited 66.7 μAh/cm^2 at 3 mA/cm^2 in 1.0 M KOH electrolyte [42]. Khan et al. reported that 1% Fe@NiO nanocomposites showed approximately 134.88 F/g at 1 A/g involution of KOH electrolyte [43]. Though various reports are accessible on NiO-based composites for supercapacitor applications in alkaline media, however, to the best of our knowledge, no reports are available in neutral media. Thus, it is important to study further in this direction using NiO-based nanocomposites.

Herein, we synthesize NiO/g-C_3N_4 nanocomposite using facile solvothermal way followed by calcination with altered molar concentration of precursors (Scheme 1) [44]. Using the three-electrode system, the electrochemical performances for supercapacitor application were carried out in neutral and alkaline electrolytes. Amidst as-prepared electrode materials, 1 : 2 molar concentration NiO/g-C_3N_4 (NO-4) shows the highest specific capacitance of 161.3 F/g at 1 A/g in 1.0 M Na_2SO_4 neutral electrolyte and 95.2 F/g at 2 mV/s at 3.0 M KOH alkaline electrolyte. The symmetric supercapacitor device has been fabricated using NO-4 electrode material and its performance is investigated in two-electrode configuration. The as-synthesized nanocomposite electrode material can be utilized as an electrochemically active candidate for energy storage applications in the near future.

2. Experimental Section

2.1. Materials Required. Nickel nitrate hexahydrate ($Ni(NO_3)_2{\cdot}6H_2O$) and tetrabutylammonium hydroxide (TBAH) were purchased from SDFCL Ltd. and Spectrochem Pvt. Ltd., respectively, pure melamine was purchased from SDFCL Ltd., anhydrous extra pure Na_2SO_4 and pure KOH pellets were received from Sisco Research Laboratories Pvt. Ltd., polyvinylidene fluoride (PVDF) was bought from Thermo Fisher Scientific India Pvt. Ltd., and ethanol was acquired from Changshu Hongsheng Fine Chemical Co., Ltd.

2.2. Synthesis of $Ni(OH)_2$ Nanoparticles. The method of solvothermal synthesis was used for the preparation of nickel hydroxide nanoparticles. In this procedure, 0.05 M (0.509 g) of nickel nitrate hexahydrate ($Ni(NO_3)_2{\cdot}6H_2O$) was added to 35 mL tetrabutylammonium hydroxide (TBAH) and continuously stirred for 20 minutes at 27°C (room temperature) in a magnetic stirrer until the formation of a homogenous mixture. Then, the resultant dispersion was shifted to a Teflon-lined stainless steel autoclave and closed up firmly. The autoclave was heated at 140°C for 12 hrs. Eventually, the autoclave is cooled down to normal laboratory conditions. The precipitate which was obtained from the above process was cleaned with deionized water and ethanol multiple times to pull out any residuals. Then, the cleaned precipitate was centrifuged at 4500 rpm for 5 min and scorched at 80°C for 48 hrs. Finally, the as-prepared nanoparticle was named NO-1.

2.3. Synthesis of g-C_3N_4 Powder. Melamine was used to synthesize g-C_3N_4 powder [45]. 5 g of melamine fine particles was kept in a crucible and calcined in a muffle furnace at 350°C for 4 hrs at a 5°C/min ramp rate, and the resultant powder was named M-1.

2.4. Preparation of NiO/g-C_3N_4 Nanocomposites by Varying Melamine Concentration. In this experiment, the NiO/g-C_3N_4 nanocomposites were prepared by differing the molar concentration of melamine powder and keeping the concentration of nickel hydroxide powder fixed. We vary the concentration of melamine such as 0.05 g, 0.1 g, 0.2 g, 0.4 g, and 0.8 g, respectively, combined with 0.1 mg of nickel hydroxide. The mixture powder was calcined at 350°C for 4 hrs at a 5°C/min ramp rate, and the resultant powder was collected (Scheme 1). The as-prepared samples were named NO-2 (1 : 0.5), NO-3 (1 : 1), NO-4 (1 : 2), NO-5 (1 : 4), and NO-6 (1 : 8), respectively.

2.5. Characterizations of Materials. The structure and phase of the crystals of synthesized nanomaterials were analyzed by the X-ray powder diffractometer (XRD)-Bruker AXS-D8 Advance, made in Germany with Cu-Kα radiation ($\lambda = 0.15406$ nm) in the 2θ range from 10° to 90°.

Field emission scanning electron microscopy was performed to find the morphologies of electrode materials. X-ray photoelectron spectroscopy (XPS) was performed by an AXIS Supra from Kratos Analytical Ltd. with Al-Kα monochromatic source to obtain the chemical composition of electrode materials.

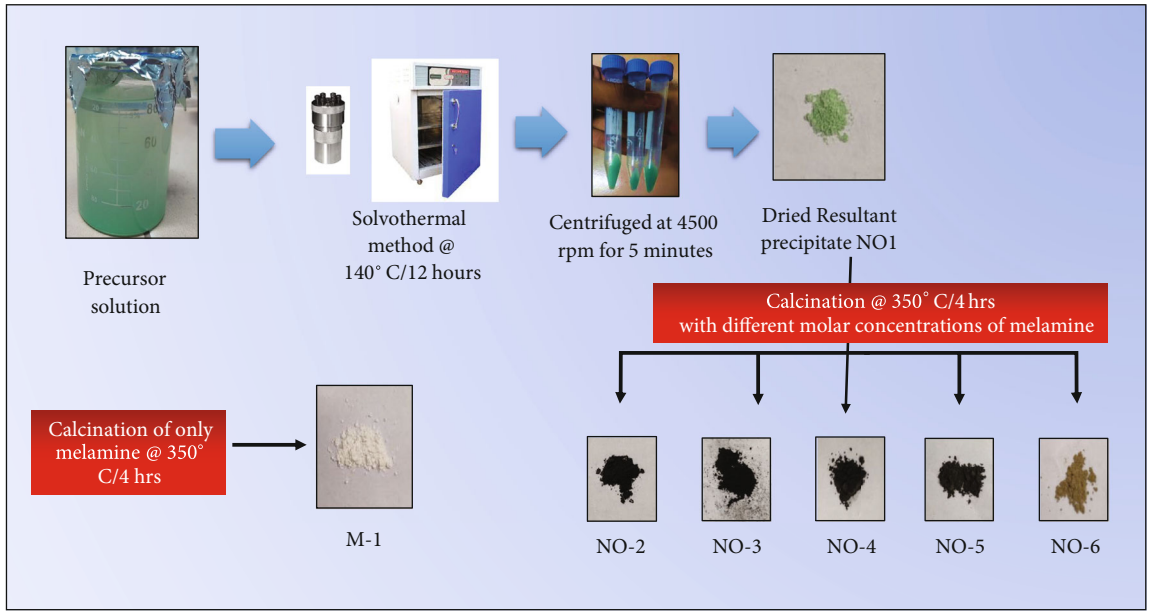

Scheme 1: Illustrative representation for the synthesis of NiO/g-C_3N_4 nanocomposite.

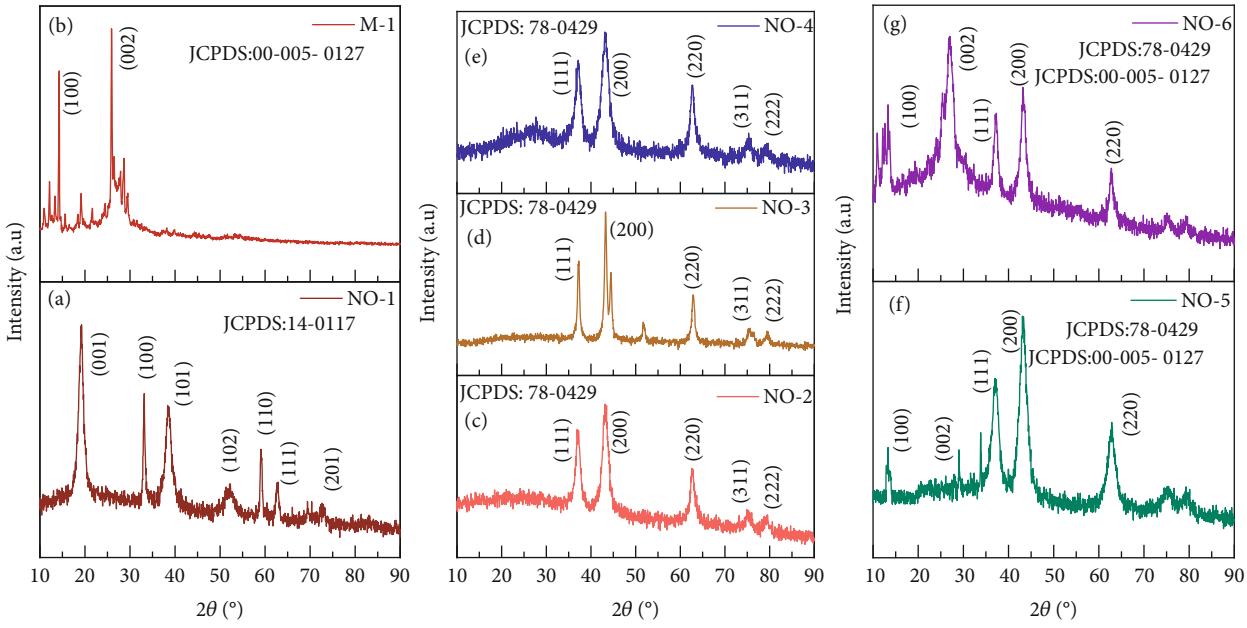

Figure 1: XRD patterns of (a) NO-1, (b) M-1, (c) NO-2 (1 : 0.5), (d) NO-3 (1 : 1), (e) NO-4 (1 : 2), (f) NO-5 (1 : 4), and (g) NO-6 (1 : 8) nanocomposites, respectively.

2.6. Electrochemical Characterization. For electrochemical performances by a three-electrode setup, NiO/g-C_3N_4 nanocomposite electrodes were wielded as working electrodes, while Ag/AgCl and platinum (Pt) wire served as reference electrodes and counter electrodes, respectively. The cyclic voltammetric study (CVD) and galvanostatic charge-discharge (GCD) analysis were performed in electrochemical workstation CHI7007E. The working electrode was prepared using the as-prepared NiO/g-C_3N_4 of mass 1 mg and binder as polyvinylidene difluoride (PVDF) mixed and finely powdered in a grinder, and hardly any drops of N-methyl 1-2 pyrrolidone (NMP) solvent are added to get ink formed. The as-produced ink was applied on a graphite sheet in an area of 10 × 10 mm^2 and heated for 5-6 hrs. For this electrochemical analysis, 1.0 M of aqueous Na_2SO_4 neutral electrolyte and 3.0 M of aqueous KOH alkaline electrolyte are used at room temperature. The electrochemical impedance spectroscopy (EIS) measurements were performed for all the electrodes in the range of frequency of 0.01 Hz–

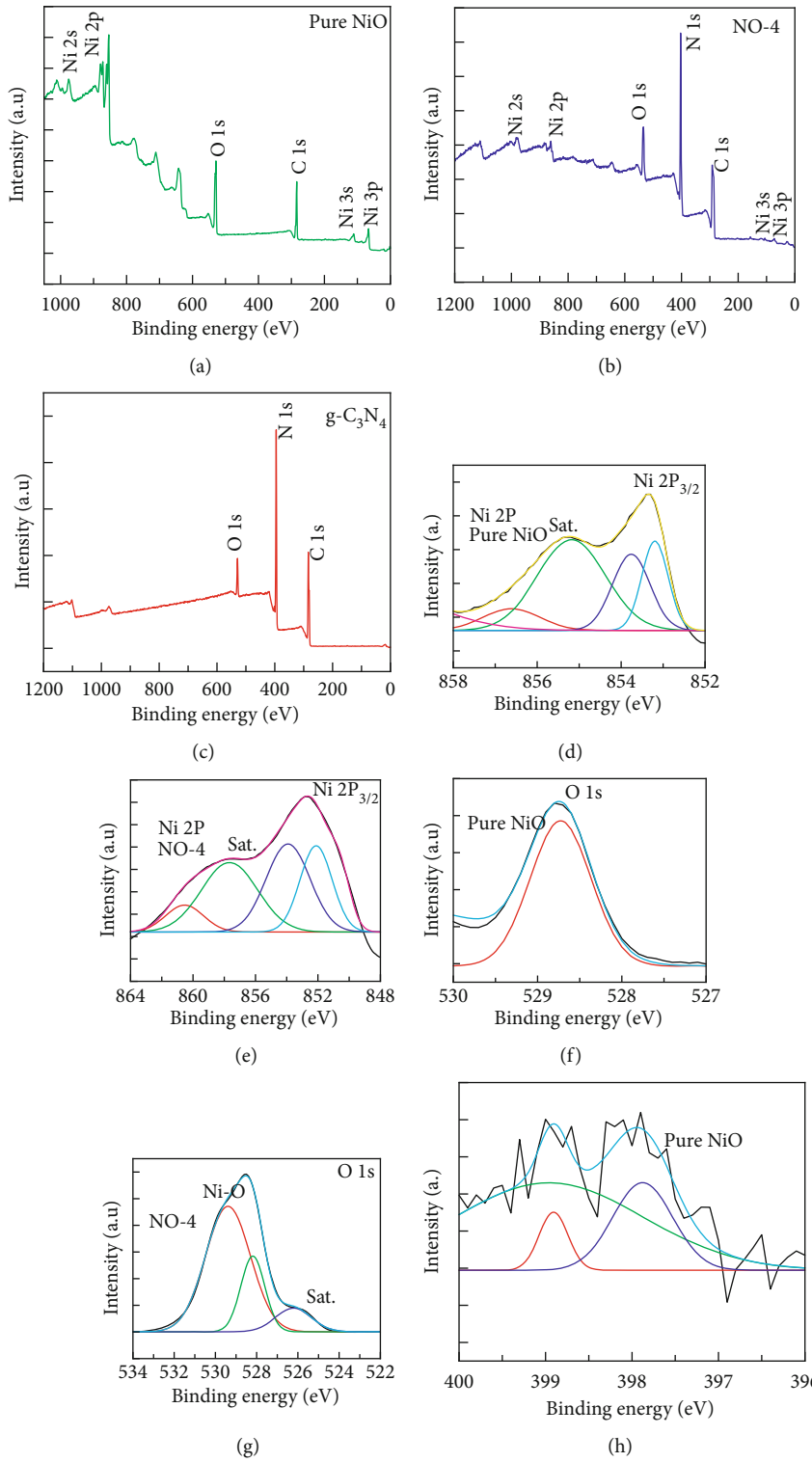

Figure 2: Continued.

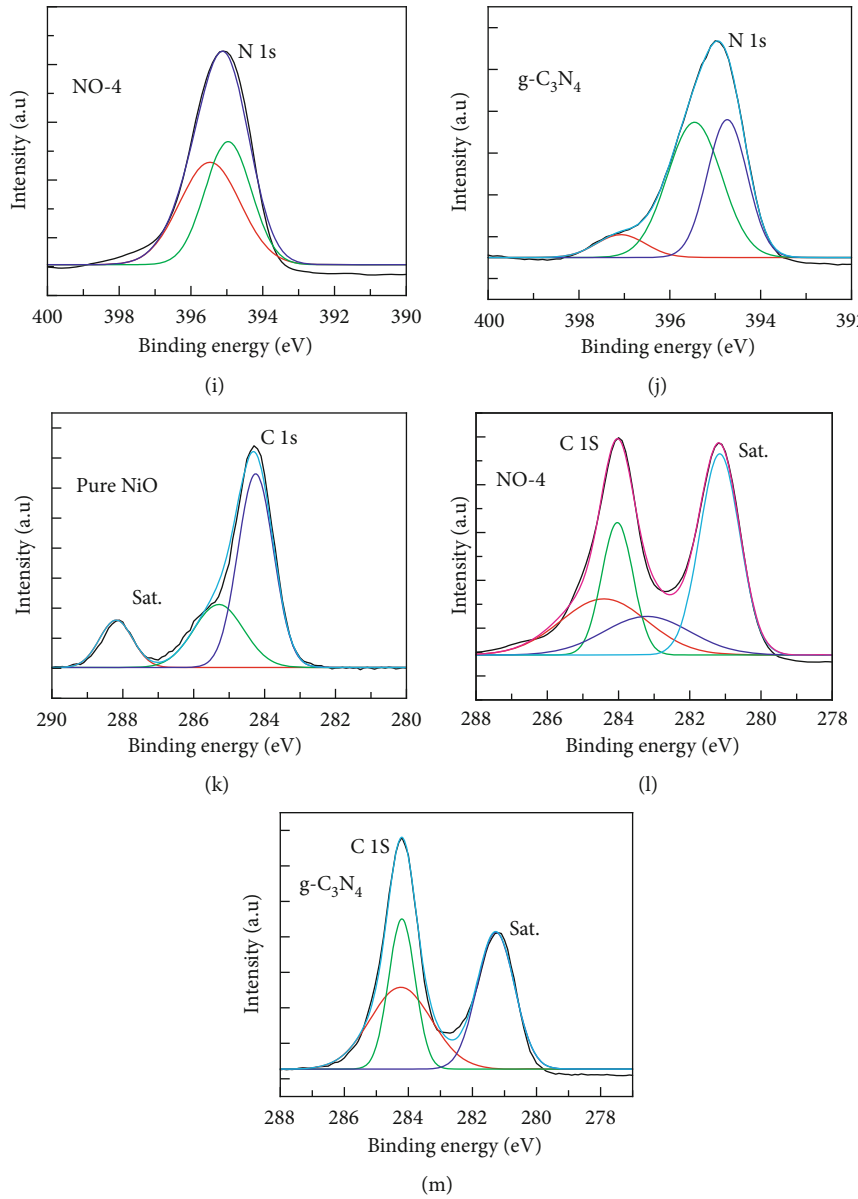

FIGURE 2: XPS wide spectra of (a) pure NiO, (b) NiO/g-C_3N_4 (NO-4), and (c) g-C_3N_4; high-resolution spectra of nickel of (d) pure NiO and (e) NiO/g-C_3N_4 (NO-4); high-resolution spectra of oxygen of (f) pure NiO and (g) NiO/g-C_3N_4 (NO-4); high-resolution spectra of nitrogen of (h) pure NiO, (i) NiO/g-C_3N_4 (NO-4), and (j) g-C_3N_4; and high-resolution spectra of carbon of (k) pure NiO, (l) NiO/g-C_3N_4 (NO-4), and (m) g-C_3N_4.

10^6 Hz using AC amplitude set to 5 mV. The equation used to calculate the specific capacitance from CV analysis in a three-electrode system is

$$C_{sp} = \frac{\int_{V_1}^{V_2} i.dV}{m\vartheta(V_2 - V_1)}, \quad (1)$$

where C_{sp} is the specific capacitance of the prepared electrodes (F/g), the numerator represents the charge totality of the electrodes, m is the mass of the electrode, ϑ is the scan rate in terms of mV/s, and $(V_2 - V_1)$ refers to the "E" of the cell. The equation used to determine the specific capacitance from CD analysis in a three-electrode setup is

$$C_{sp} = \frac{i.t}{m.\Delta V}, \quad (2)$$

where C_{sp} is the specific capacitance of the prepared electrodes (F/g), i is the current in terms of A, t is the discharging time, m is the mass of the electrode, and ΔV is the window of the potential of the cell.

3. Results and Discussions

3.1. Structural Analysis. The structure of a crystal, structural behavior, phase structure, and purity were analyzed using

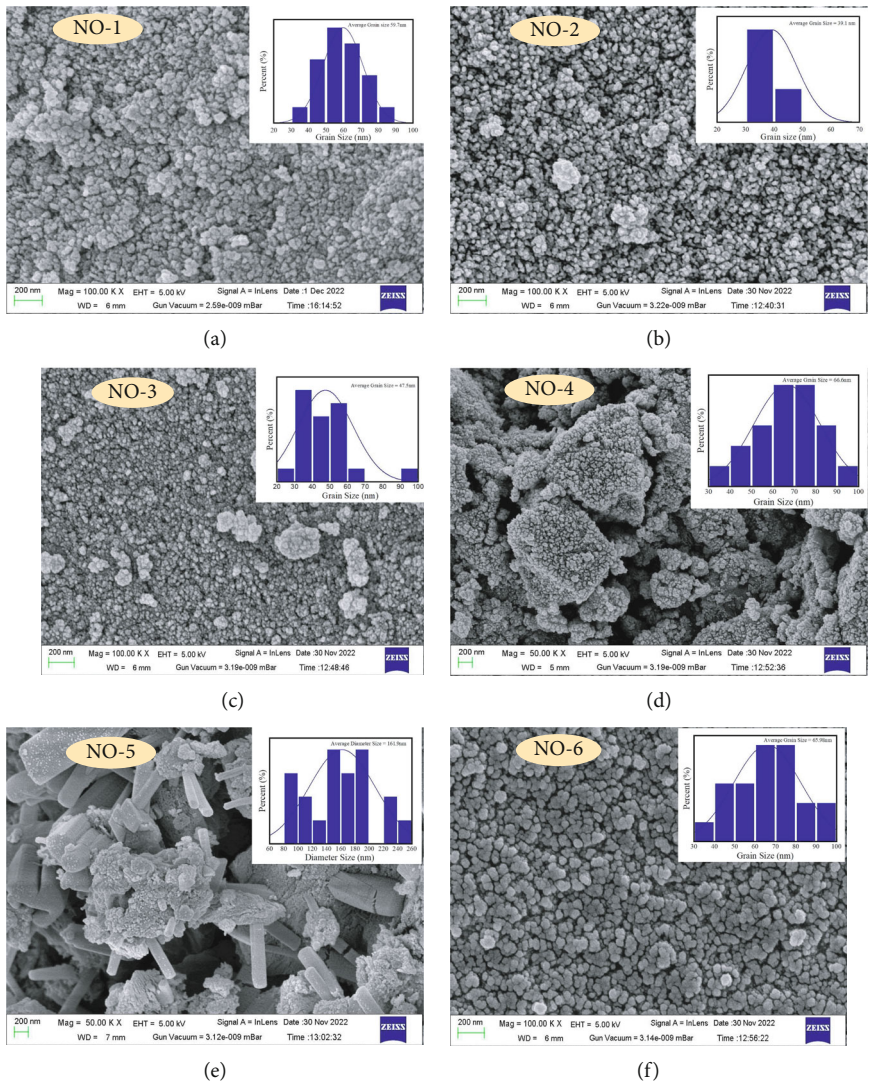

FIGURE 3: FE-SEM images of (a) NO-1, (b) NO-2 (1 : 0.5), (c) NO-3 (1 : 1), (d) NO-4 (1 : 2), (e) NO-5 (1 : 4), and (f) NO-6 (1 : 8), respectively.

powder X-ray diffraction of $Ni(OH)_2$ and $NiO/g\text{-}C_3N_4$ nanostructures. Figure 1(a) shows the XRD pattern of $Ni(OH)_2$ nanoparticles. As illustrated in Figure 1(a), the 2θ peaks located at 19.14°, 33.16°, 38.47°, 52.36°, 59.1°, 62.7°, and 73.26° agree with the (001), (100), (101), (102), (110), (111), and (201) crystal facets of $Ni(OH)_2$ (NO-1). All the characteristic diffraction peaks were indexed with the standard JCPDS file (JCPDS no. 14-0117). Figure 1(b) shows the 2θ diffraction peaks of the $g\text{-}C_3N_4$ (M-1) which is prepared by calcinating the pure melamine at the temperature of 350°C for 4 hrs at 5°C/min ramp rate located at 14.28° and 25.9° which are corresponding to crystal faces (100) and (002). All the major diffraction peaks were indexed with the standard JCPDS file (JCPDS no. 05-005-0127). No other residue peaks are found, which suggests that it has well phase purity. Further, to understand the influence of varying molar concentrations of melamine with respect to NO-1, the XRD patterns of samples NO-2 (1 : 0.5), NO-3 (1 : 1), NO-4 (1 : 2), NO-5 (1 : 4), and NO-6 (1 : 8) are shown in Figures 1(c)–1(g). In Figures 1(c)–1(e), the 2θ diffraction peaks of NO-2 (1 : 0.5), NO-3 (1 : 1), and NO-4 (1 : 2) are similar and match with the cubic nickel oxide diffraction peaks situated at 36.9°, 43.48°, 62.89°, 75.5°, and 79.34°, agreeing with the crystal planes, namely, (111), (200), (220), (311), and (222), and there is no major swap in the positions of peaks of the samples. The high-intensity peaks of these samples showcase the good crystalline characteristic of nanostructures. All the major diffraction peaks were indexed with the standard JCPDS file (JCPDS no. 78-0429). NO-2 (1 : 0.5) and NO-3 (1 : 1) show no other characteristic peaks and were found to be not influenced by the incorporation of $g\text{-}C_3N_4$, due to the small amount of melamine used during calcination. However, in Figure 1(e), NO-4 (1 : 2) reveals small intense peaks of $g\text{-}C_3N_4$ which are not indexed. In Figures 1(f) and 1(g), the XRD patterns of NO-5 (1 : 4) and NO-6 (1 : 8) shows the crystal peaks of both cubic NiO and $g\text{-}C_3N_4$. In NO-6 (1:8), the peak corresponding to (002) crystal face belongs to $g\text{-}C_3N_4$ and it is higly intense than $g\text{-}C_3N_4$ peak of NO-5 (1:4) nanocomposite.

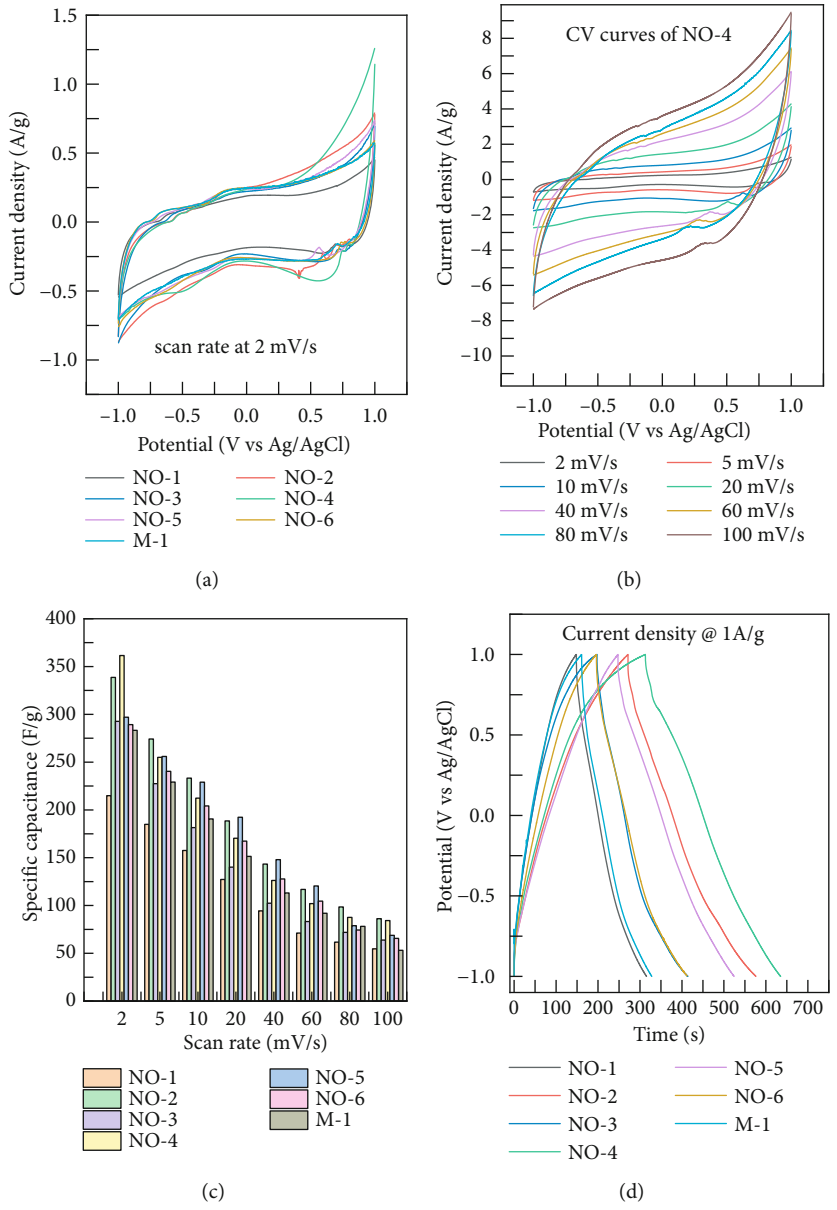

Figure 4: Continued.

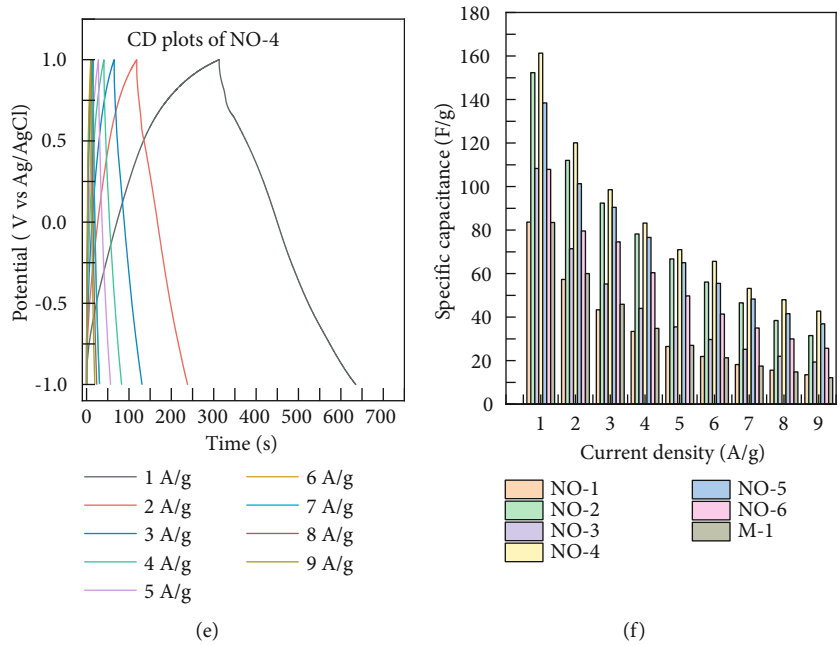

Figure 4: (a) CV plots of all electrodes at 2 mV/s, (b) CV plots of NO-4 (1 : 2) at scan rates of 2-100 mV/s, (c) specific capacitance of all electrode materials as a function of scan rates, (d) CD plots of all electrodes at 1 A/g, (e) CD plots of NO-4 (1 : 2) at scan rates of 1-9 A/g, and (f) specific capacitance of all electrodes as a function of current densities.

3.2. Chemical Composition Analysis. XPS is operated to assess the elemental composition and its states of NiO/g-C_3N_4 and g-C_3N_4. Figures 2(a)–2(c) give the XPS full survey spectrum of NiO, NiO/g-C_3N_4, and g-C_3N_4, respectively. The survey spectrum of NO-4 (NiO/g-C_3N_4) divulges the presence of elements such as nickel (Ni), oxygen (O), nitrogen (N), and carbon (C), suggesting the successful formation of the nanocomposite. On the other hand, nickel, oxygen, and surface impurity carbon are present in NO-4 (Figure 2(b)), and for the g-C_3N_4 survey spectrum, nitrogen, oxygen, and carbon were observed (Figure 2(c)), confirming the formation of the samples. Figure 2(e) shows the deconvoluted high-resolution narrow scan spectrum of Ni 2p, in which the high-intensity peak of Ni $2p_{3/2}$ is located at a binding energy of 852.8 eV. Also, the low-intensity satellite humps are observed at 857.6 eV. This validates the presence of the +2-oxidation state of Ni, and it is consistent with the previous report [46, 47]. Figure 2(g) shows the deconvoluted high-resolution scan spectra of O 1s. The high-intensity bumps revealed at a binding energy of 528.9 eV authenticate the presence of the Ni-O bond, and the less intense peak is attributed to satellite humps confirming the O^{2-} oxidation state. Furthermore, Figures 2(l) and 2(m) show that the deconvoluted high-resolution spectrum C 1s reveals the peaks at a binding energy of 284.1 eV, and it is aroused from carbon (C-C and C=C) bonds. The other peak at 281.2 eV is attributed to satellite humps [48–50]. Also, the high-resolution scan spectrum of N 1s in Figures 2(i) and 2(j) shows the intensity peak at binding energy at 395.2 eV with no other intensity bumps. It is to be observed that a negligible nitrogen peak was found for NiO (Figure 2(h)) whereas a strong peak for NiO/g-C_3N_4 and g-C_3N_4. Hence, the successful incorporation of nitrogen in NO-4 confirms the formation of the nanocomposite.

3.3. Morphology Analysis. The surface morphologies of the synthesized samples (Figure 3) were analyzed by optimizing the concentration of g-C_3N_4. Figure S1 (Supporting Information, SI) represents the FESEM image of bare g-C_3N_4 nanorods with agglomerated nanoparticle-like mixed morphology noticed, and the average diameter is measured to be 97 nm (inset of Figure S1). Nickel hydroxide (NO-1) synthesized by a solvothermal process using TBAH as solvent shows nanoparticle-like morphology with an estimated average grain size of 59.7 nm (Figure 3(a)). Additionally, to study the role of graphitic nitride, the nanocomposite with 0.05 g, 0.1 g, 0.2 g, 0.4 g, and 0.8 g, respectively, combined with 0.1 g of nickel hydroxide was synthesized via heat treatment, and their morphologies were studied. Figure 3(b) shows the nanoparticle-like morphology for NO-2 (1 : 0.5) nanocomposite with an average grain size of 39.1 nm. Further, NO-3 (1 : 1) and NO-4 (1 : 2) show slightly agglomerated nanoparticle-like morphology (Figures 3(c) and 3(d)) with mean grain sizes of 66.6 nm and 47.5 nm, respectively. Moreover, the NO-5 (1 : 4) nanocomposite (Figure 3(e)) shows the agglomerated nanorod-like structures along with nanoparticles, and the average diameter was found to be 161.9 nm. The change in the morphology of NO-5 could be ascribed to the initialization of a moderate concentration of melamine decomposition into the nickel oxide surfaces to form NiO/g-C_3N_4 under heat treatment. Further increasing the concentration of melamine, in NO-6 (1 : 8), g-C_3N_4 is found to be dominant over NiO and retained the morphology of g-C_3N_4 as agglomerated nanoparticles (Figure 3(f)) with an average grain size of 66 nm in NiO/g-C_3N_4 [51]. The smaller particle size of NO-4 suggests a large surface area with a greater number of active sites and indicating to deliver a good electrochemical performance.

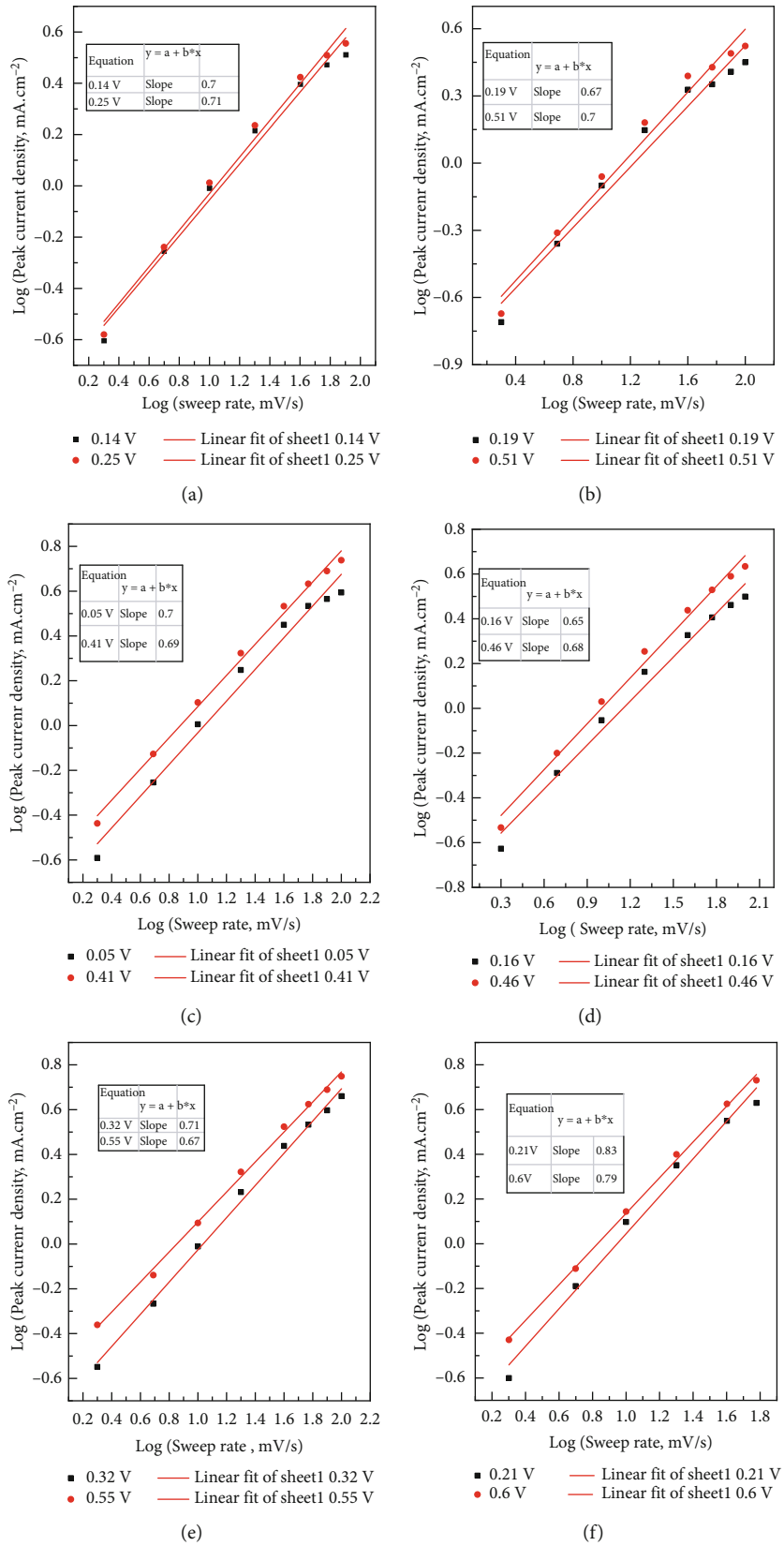

Figure 5: Continued.

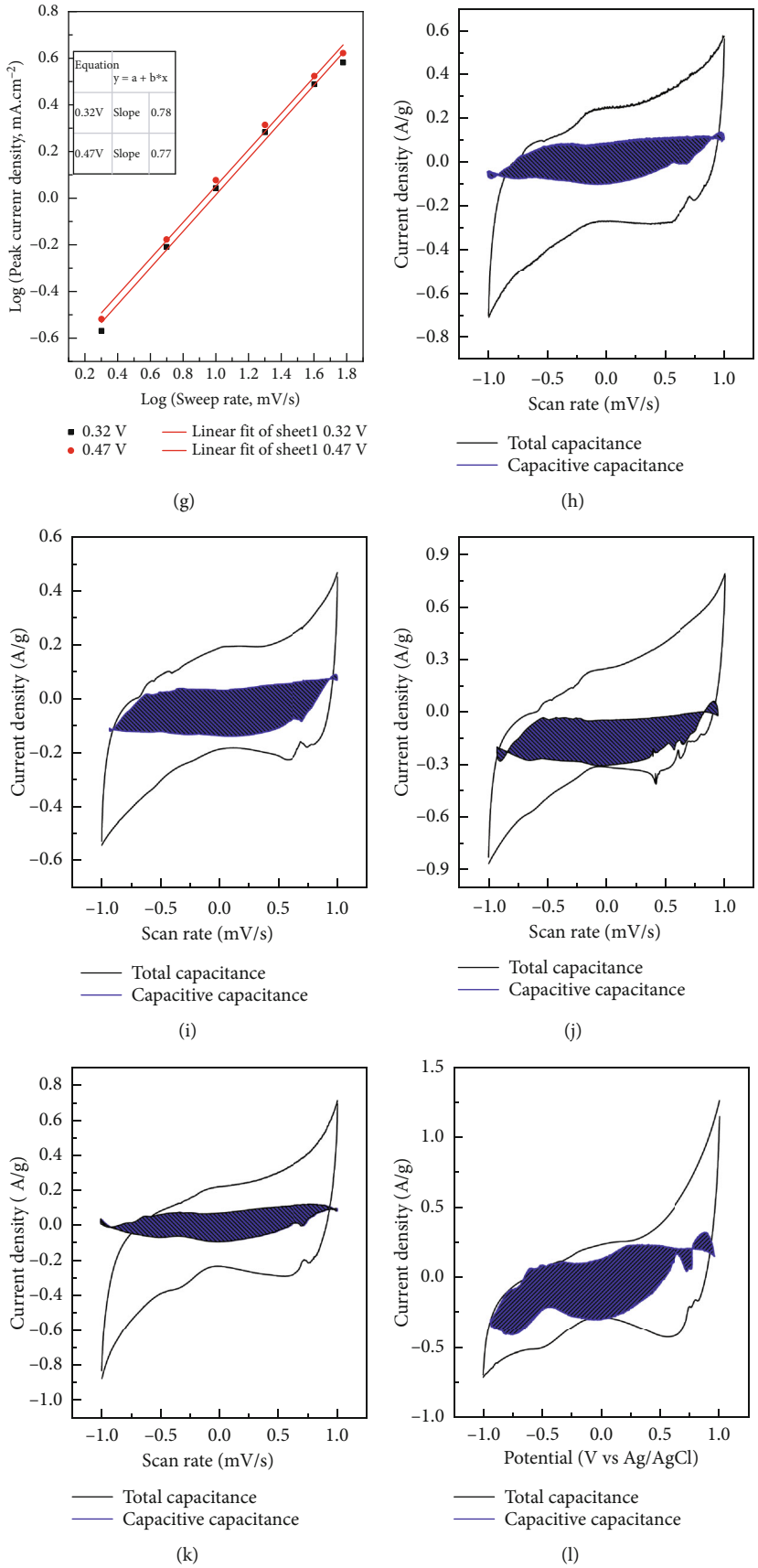

Figure 5: Continued.

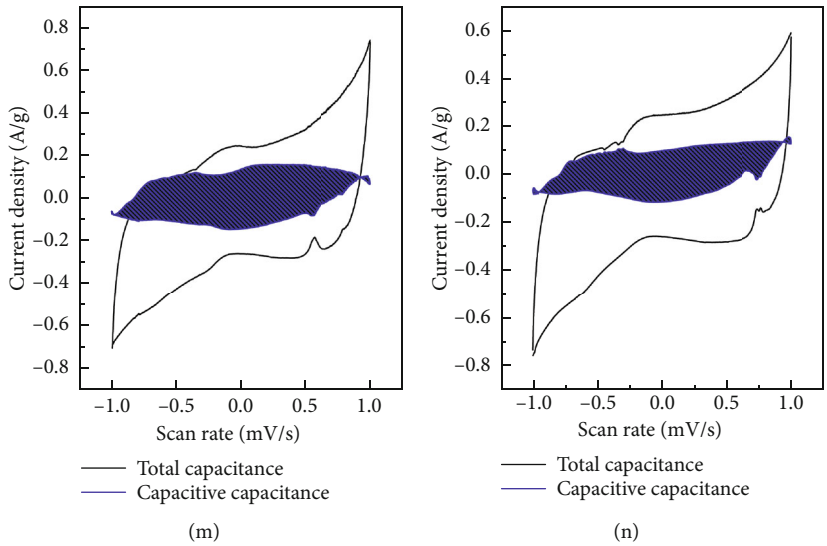

Figure 5: The plot of logarithmic current density vs. scan rates of (a) M-1, (b) NO-1, (c) NO-2, (d) NO-3, (e) NO-4, (f) NO-5, and (g) NO-6. The plot of capacitive and diffusion contribution at 2 mV/s: (h) M-1, (i) NO-1, (j) NO-2, (k) NO-3, (l) NO-4, (m) NO-5, and (n) NO-6, respectively.

3.4. Electrochemical Analysis. To determine the electrochemical capacitance of the synthesized electrodes, a three-electrode configuration was configured using Ag/AgCl, Pt wire, and fabricated electrode material painted on a graphite sheet as a reference, counter, and working electrode, respectively, to study the various electrochemical analysis. The cyclic voltammetry study (CV), galvanic charge-discharge analysis (GCD), and EIS investigation were carried out in 1.0 M Na_2SO_4 neutral and 3.0 M KOH alkaline electrolyte. Figure 4(a) reveals the CV curves of all electrodes at a fixed scan rate of 2 mV/s in neutral electrolytes with a range of potential of 2.0 V (-1.0 V to 1.0 V). It is to be observed that all electrode materials show a quasirectangular character with a duo of redox peaks (Figure 4(a)), validating the pseudocapacitive behavior of the prepared materials. The voltammetric area of NiO/g-C_3N_4 (NO-4) was observed to be larger compared to all samples, demonstrating higher specific capacitance of the NO-4 electrode. The specific capacitance of as-synthesized electrode materials such as M-1, NO-1, NO-2 (1 : 0.5), NO-3 (1 : 1), NO-4 (1 : 2), NO-5 (1 : 4), and NO-6 (1 : 8) is 283.23 F/g, 214.9 F/g, 338.68 F/g, 292.7 F/g, 361.53 F/g, 296.9 F/g, and 289.26 F/g, respectively, at a scan rate of 2 mV/s. As seen, the specific capacitance of NO-4 (1 : 2) nanocomposite shows a dominant specific capacitance amidst all electrodes due to its larger voltammetric area and smaller particle size. Figure 4(b) showcases the CV curves of NO-4 (1 : 2) nanocomposite at different scan rates. The specific capacitance at scan rates of 5 mV/s, 10 mV/s, 20 mV/s, 40 mV/s, 60 mV/s, 80 mV/s, and 100 mV/s is 255 F/g, 212.4 F/g, 170.39 F/g, 126.16 F/g, 101.9 F/g, 87.49 F/g, and 84.21 F/g, respectively. It has been observed that, as the scan rate increases, the capacitance of the NO-4 (1 : 2) electrode decreases significantly without a change in the shapes of voltammogram curves, indicating high stability of the electrode. At low scan rates, the majority of active electrode material in the NO-4 (1 : 2) electrode takes part in redox reactions permitting the charges to drive deep, which attributes to high specific capacitance and vice versa. The CV profile of M-1 (Figure S2a, SI), NO-1 (Figure S2b, SI), NO-2 (Figure S2c, SI), NO-3 (Figure S2d, SI), NO-5 (Figure S2e, SI), and NO-6 (Figure S2f, SI) at diverse scan rates (2-100 mV/s) is presented in Figure S2. Moreover, the calculated specific capacitance of all the electrodes as a function of scan rates (Figure 4(c)) reveals that the NO-4 (1 : 2) electrode material has the greater specific capacitance at all sweep rates and this is attributed to its smaller particle size. Furthermore, the galvanic CD analysis of all the electrodes has been studied at current densities of 1 A/g with a window of the potential of 2 V in a three-electrode configuration under neutral media. The charge-discharge plots of all electrodes at a current density of 1 A/g show a nonlinear triangular profile (Figure 4(d)) proving the pseudocapacitive behaviors of electrodes. The electrode materials such as M-1, NO-1, NO-2 (1 : 0.5), NO-3 (1 : 1), NO-4 (1 : 2), NO-5 (1 : 4), and NO-6 (1 : 8) show specific capacitance of 83.5 F/g, 83.7 F/g, 152.35 F/g, 108.3 F/g, 161.3 F/g, 138.4 F/g, and 107.9 F/g, respectively, at a current density of 1 A/g. Note that NO-4 (1 : 2) shows the greatest specific capacitance of 161.3 F/g at 1 A/g than other electrodes. Further, the specific capacitance of NO-4 electrode at 2 A/g, 3 A/g, 4 A/g, 5 A/g, 6 A/g, 8 A/g, and 9 A/g is calculated as 120.1 F/g, 98.55 F/g, 83.2 F/g, 71 F/g, 45.6 F/g, 53.2 F/g, 48 F/g, and 42.75 F/g, respectively (Figure 4(e)). Consistent decrement of the specific capacitance is owed to the less transportation of charges in the active region when the current density increases. Figure S3 shows the charge-discharge profile of M-1 (Figure S3a, SI), NO-1 (Figure S3b, SI), NO-2 (Figure S3c, SI), NO-3 (Figure S3d, SI), NO-5 (Figure S3e, SI), and NO-6 (Figure S3f, SI) at various current densities (1-9 A/g). Moreover, the specific capacitance of all the electrodes varying in order with current densities is shown in

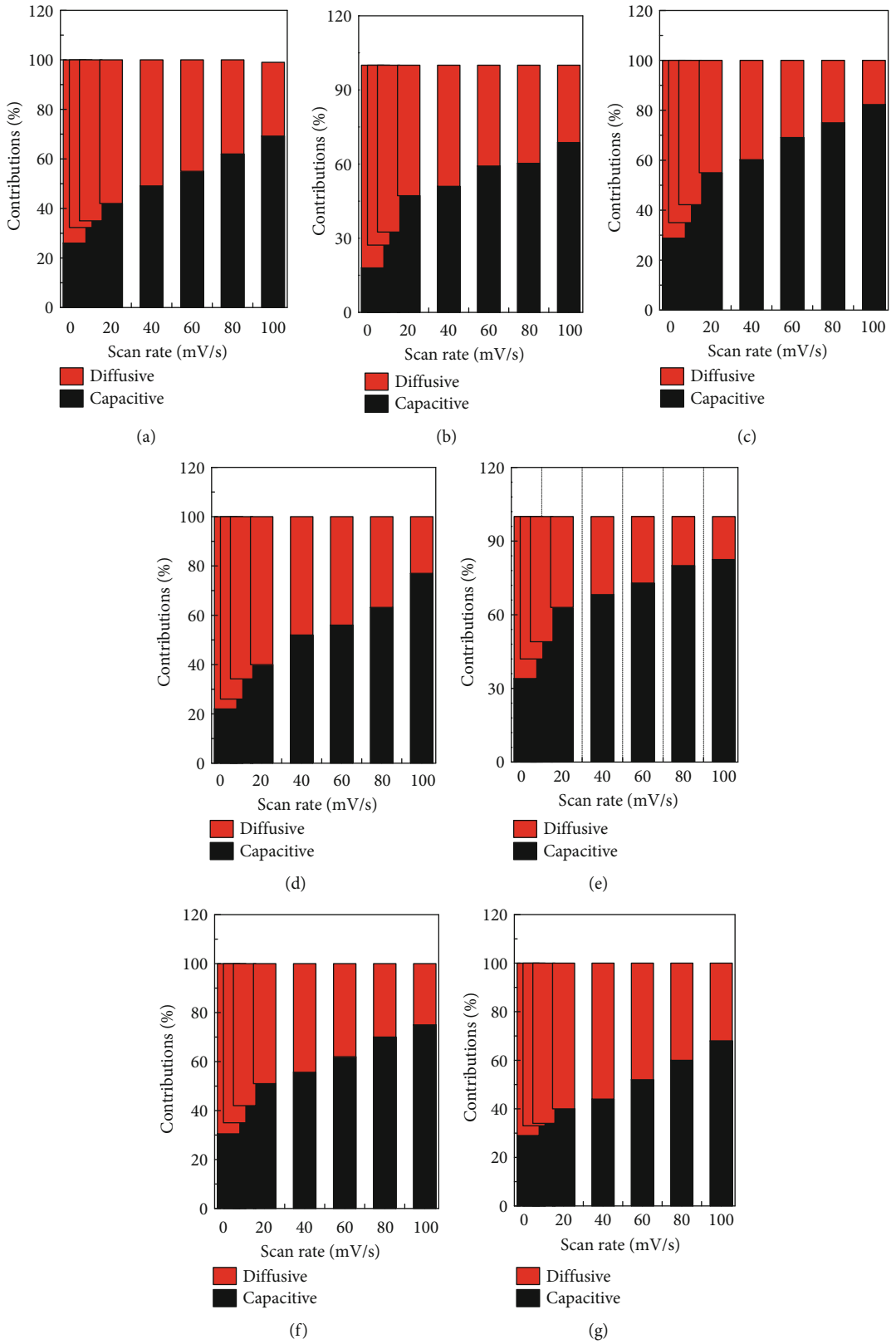

Figure 6: Column plot of the contribution of capacitive and diffusive vs. different scan rates of the synthesized electrodes: (a) M-1, (b) NO-1, (c) NO-2, (d) NO-3, (e) NO-4, (f) NO-5, and (g) NO-6.

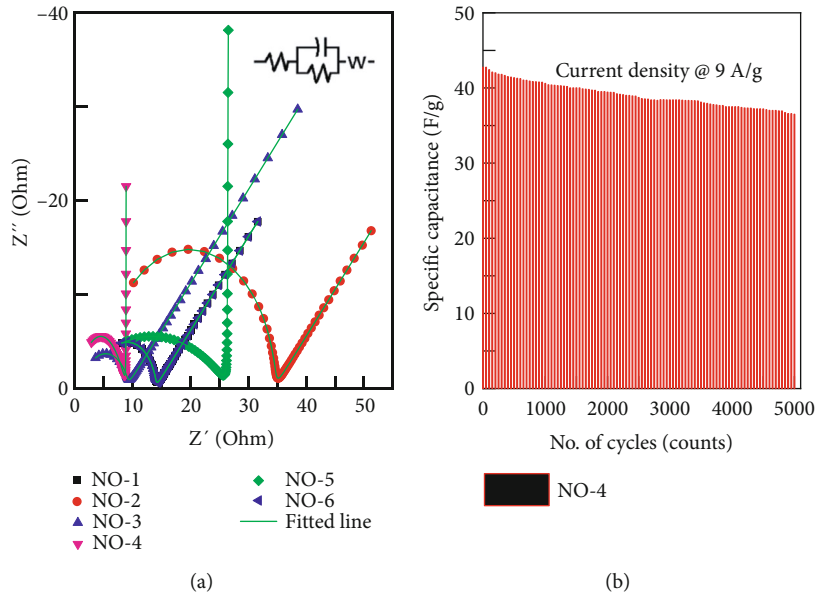

FIGURE 7: (a) EIS plot of NO-1, NO-2 (1 : 0.5), NO-3 (1 : 1), NO-4 (1 : 2), NO-5 (1 : 4), and NO-6 (1 : 8) and (b) stability plot of NO-4 (1 : 2) at 9 A/g for 5000 cycles.

Figure 4(f). Among all the electrodes, NO-4 (1 : 2) exhibits the higher specific capacitance in all current densities under 1.0 M Na_2SO_4. Hence, NO-4 (1 : 2) is the best promising electrode compared to other reported NiO-based electrodes (Table S1, SI) [52–56]. Furthermore, to acknowledge the electrochemical characteristic of the best electrode NO-4 (1 : 2) in alkaline media, the electrochemical performances are performed in 3.0 M KOH electrolyte (Figure S4, SI) with a range of potential of 2 V. Figure S4a illustrates the CV curves of NO-4 (1 : 2) in KOH electrolyte, and the specific capacitance measured at scan rates of 2 mV/s, 5 mV/s, 10 mV/s, 20 mV/s, 40 mV/s, 60 mV/s, 80 mV/s, and 100 mV/s are 95.22 F/g, 66.16 F/g, 49.34 F/g, 34.25 F/g, 21.64 F/g, 16.13 F/g, 12.41 F/g, and 8.98 F/g respectively. The specific capacitance of the NO-4 (1 : 2) electrode in the KOH electrolyte (Figure S4b, SI) is significantly less than in the Na_2SO_4 electrolyte (Figure 4(c)). Since the K^+ ions are larger in size, results in the capability of desertion and insertion are less when compared to Na^+ in neutral Na_2SO_4 electrolyte [57].

To understand the charge storage behavior of as-synthesized samples, we further analyzed the electrokinetics by using Dunn's method. The charge totality of electrodes which shows pseudocapacitive behavior can be stored in two different ways, namely, (i) capacitive and (ii) diffusive. According to Dunn's equations,

$$i = a.v^b,$$
$$\log i = \log a + b.\log v, \tag{3}$$

where "i" and "v" shows the current density (A/g) and sweep rates (mV/s), respectively. The capacitive and diffusive contributions of the pseudocapacitive electrodes were measured by the derived "b" value from the equation above [58, 59]. For the absolute pseudocapacitive and diffusive character to store total charge, the value of "b" should be 1 and 0.5 for capacitive and diffusive, respectively. The estimated "b" value of prepared samples for cathodic and anodic peaks is 0.7 and 0.71 (M-1; Figure 5(a)), 0.67 and 0.7 (NO-1; Figure 5(b)), 0.7 and 0.69 (NO-2; Figure 5(c)), 0.65 and 0.68 (NO-3; Figure 5(d)), 0.71 and 0.67 (NO-4; Figure 5(e)), 0.83 and 0.79 (NO-5; Figure 5(f)), and 0.78 and 0.77 (NO-6; Figure 5(g)), respectively. The entire charge for all the electrodes is stored (Figures 5(a)–5(g)) and was found to be a combination of capacitive and diffusive benefactions. The extensive electrokinetic investigation was further examined using CV plots of all synthesized electrode materials. Peak currents in CV curves fluctuate with the scan rate that is regulated by diffusive and capacitive processes mediated by a redox reaction. Several approaches for denoising diffusive and capacitive control processes for pseudocapacitive electrodes have been reported [60, 61]. Brezesinski et al., in particular, proposed a generalized equation for electrokinetic studies employing CV studies at various sweep rates. The normalized equations are given below [62]:

$$i(V) = k_1 v + k_2 v^{1/2},$$
$$\frac{i(V)}{V^{1/2}} = k_1 v^{1/2} + k_2. \tag{4}$$

In this equation, "V" represents the potential, "v" represents the scan rate, and "k_1" and "k_2" represents the constants and are used to calculate the capacitive and diffusive currents of CV plots for prepared pseudocapacitive electrode materials.

The CV plots of capacitive (shaded area) and diffusive contribution of all electrode materials are estimated to be 26% and 74% (M-1; Figure 5(h)), 18% and 82% (NO-1; Figure 5(i)), 28% and 72% (NO-2; Figure 5(j)), 22% and 78% (NO-3; Figure 5(k)), 34% and 66% (NO-4; Figure 5(l)), 31%

Table 1: R_{ct}, R_s, and W of electrode materials.

S. no.	Electrode material	R_{ct} (Ω)	R_s (Ω)	W (Ω)
1	NO-1	9.244	5.074	0.01151
2	NO-2 (1 : 0.5)	29.53	4.944	0.01681
3	NO-3 (1 : 1)	7.25	6.596	0.009494
4	NO-4 (1 : 2)	6.71	3.093	0.0002829
5	NO-5 (1 : 4)	26.74	9.65	0.004124
6	NO-6 (1 : 8)	9.8	4.043	0.01587

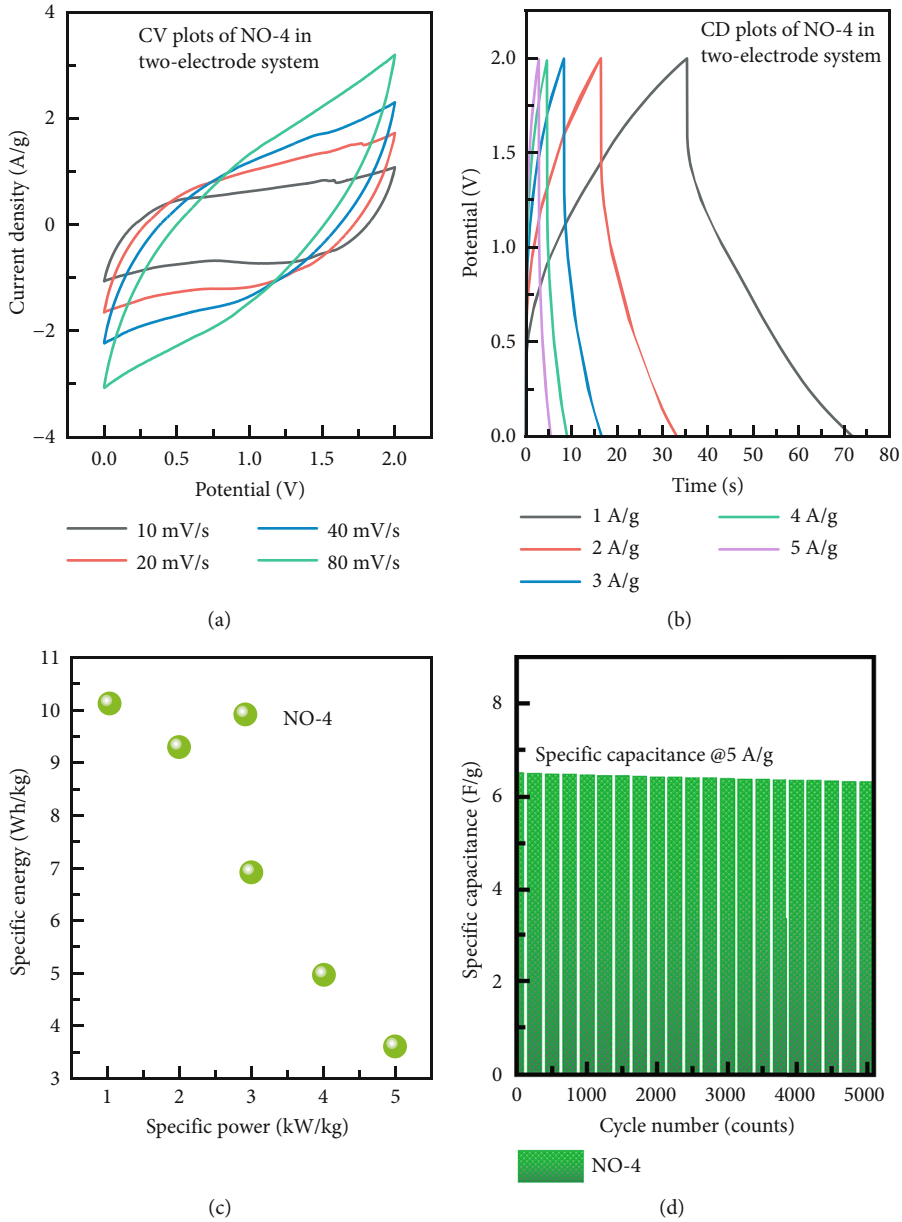

Figure 8: (a) CV plots of NO-4 at various scan rates in a two-electrode system. (b) CD plots of NO-4 at various current densities in a two-electrode system. (c) The Ragone plot of NO-4//NO-4 SSD. (d) Cyclic stability plot of the NO-4//NO-4 SSD device.

and 69% (NO-5; Figure 5(m)), and 29% and 71% (NO-6; Figure 5(n)), respectively, at 2 mV/s scan rate by Dunn's method. The maximum contribution of NO-4 is observed from capacitive behavior than other NiO/g-C_3N_4 electrodes, which are accredited to higher specific capacitance.

Further, the capacitive and diffusive contributions of all the prepared electrode materials are measured for diverse scan rates (2-100 mV/s) using CV curves. Figure 6 shows the column plot illustration of the contribution of the capacitive and diffusive of all prepared electrode materials. For all scan speeds, the NO-4 electrode has a highest capacitive contribution, implying greater longevity and good electrochemical performances.

Moreover, the electrochemical impedance spectroscopy (EIS) analysis helps to determine the resistance of charge transfer (R_{ct}) of each prepared electrode. Figure 7(a) shows the Nyquist plot of all the electrodes. From the figures, at the lower frequencies, the radius of the depressed semicircle is attributed to the charge transfer resistance (R_{ct}), and the linear straight line at high frequency corresponds to the Warburg resistance (W) that is due to diffusion of ions in the interface of the electrolyte and the active electrode [63]. The observed depressed semicircle could be ascribed to the increment of relaxation time and IR drop (observed from CD plot (Figure 4(d))) with respect to the electrode and electrolyte interface [64, 65]. The resistance of charge transfer (R_{ct}) with the resistance of the solution (R_s) and the Warburg resistance (W) of all the synthesized electrode materials such as NO-1, NO-2 (1 : 0.5), NO-3 (1 : 1), NO-4 (1 : 2), NO-5 (1 : 4), and NO-6 (1 : 8) is tabulated in Table 1. The NO-4 (1 : 2) shows lower R_{ct} and R_s, hence providing higher conductivity which helps to gain higher electrochemical performances [66]. Further stability plays an important parameter of active electrodes to understand the practical application. Figure 7(b) demonstrates the long-term charge-discharge test for 5000 cycles at 9 A/g under neutral electrolyte. The specific capacitance for the 1st CD cycle was measured to be 42.75 F/g at 9 A/g that was observed to be 36.5 F/g at 9 A/g after 5000 CD cycles. A small change in specific capacitance for NO-4 suggests a prospective contender for upcoming energy storage devices.

3.5. Symmetric Supercapacitor Device Configuration. The performance of the as-prepared electroactive material for supercapacitor application is examined in the neutral electrolyte of 1.0 M Na_2SO_4 through a symmetrically configured two-electrode arrangement. Since NO-4 showed a maximum specific capacitance in a three-electrode system, we choose to fabricate NO-4 as a NO-4//NO-4 symmetric supercapacitor device (SSD) for the two-electrode system with an electrode mass of 1 mg. The CV profiles of NO-4//NO-4 SSD (Figure 8(a)) at various scan rates of 10 mV/s, 20 mV/s, 40 mV/s, and 80 mV/s were captured and exhibited the specific capacitance of 128.3 F/g, 100.8 F/g, 62.64 F/g, and 40.23 F/g, respectively. From CV profile, a rectangular voltammetric area for as-fabricated SSD is observed in a stable potential window of 0 V-2.0 V [67, 68]. Furthermore, the GCD analysis of NO-4//NO-4 has been carried out in the potential of 2.0 V, and the results are depicted in Figure 8(b). The NO-4//NO-4 SSD reveals specific capacitance of 18.28 F/g, 16.8 F/g, 12.45 F/g, 8.94 F/g, and 6.5 F/g at a current density of 1 A/g, 2 A/g, 3 A/g, 4 A/g, and 5 A/g, respectively. The Ragone plot which helps to compare the performance of the device [69] of NO-4//NO-4 SSD is shown in Figure 8(c), and upon observation at the lowest current density of 1 A/g, the maximal energy density of 10.13 Wh/kg is revealed with a paralleling power density of 1.01 kW/kg. As shown in Figure 8(d), continuous 5000 charge and discharge cycles have been performed for the NO-4//NO-4 SSD device at a current density of 5 A/g. It showed a capacitance retention of 96% after 5000 charge-discharge cycles.

4. Conclusion

In this investigation, NiO/g-C_3N_4 nanocomposites were synthesized via facile synthesis for supercapacitor applications. We have found that varying the molar concentration of the g-C_3N_4 has a direct effect on the activities of electrochemical and charge-storing performances. Compared with other synthesized electrodes, NO-4 (1 : 2) nanocomposites are dominant and show a specific capacitance of 161.3 F/g at a current density of 1 A/g and a specific capacitance of 361.53 F/g at a scan rate of 2 mV/s under Na_2SO_4 neutral electrolyte. Also, under the KOH alkaline electrolyte, the best material shows a specific capacitance of 95.22 F/g at a scan rate of 2 mV/s. By investigating the two-electrode performance of NO-4//NO-4 SSD, it showed a specific capacitance of 18.23 at a current density of 1 A/g with an energy density of 10.13 Wh/kg and a power density of 1.01 kW/kg. The cyclic stability of the device is measured after 5000 cycles, and it shows a specific capacitance retention of 96%. Hence, the NiO/g-C_3N_4 with a molar concentration of 1 : 2 ratio promises a potential electrode material for the upcoming applications in supercapacitors due to its smaller particle size, lower charge transfer resistance, and higher capacitive contribution. Also, from the electrokinetic analysis, it is obvious that the capacitive and diffusive actions played a crucial role in the high charge storage performance of the best electrode.

Data Availability

Data is available upon appropriate request from the corresponding authors.

Disclosure

Preprint details are available on this site: doi:10.2139/ssrn.4396592.

Conflicts of Interest

The authors declare no competing interests.

Acknowledgments

This research was supported by the Basic Science Research Program through the National Research Foundation of Korea (NRF) funded by the Ministry of Science, ICT and Future Planning (2021R1A2C2091497).

Supplementary Materials

Figure S1: FE-SEM image of pure g-C_3N_4 (M-1) sample. Inset shows the average particle size distribution. Figure S2: CV profiles of the samples at various scan rates: (a) M-1, (b) NO-1, (c) NO-2, (d) NO-3, (e) NO-5, and (f) NO-6, respectively. Figure S3: CD profiles of the samples at various current densities: (a) M-1, (b) NO-1, (c) NO-2, (d) NO-3, (e) NO-5, and (f) NO-6, respectively. Figure S4: (a) CV curves of NO-4 (1 : 2) at scan rates of 2-100 mV/s under 3.0 M KOH electrolyte and (b) specific capacitance of NO-4 (1 : 2) nanocomposites as a function of scan rates. Table S1: specific capacitance of the NiO-based nanocomposites. *(Supplementary Materials)*

References

[1] T. Meng, P. P. Ma, J. L. Chang, Z. H. Wang, and T. Z. Ren, "The electrochemical capacitive behaviors of NiO nanoparticles," *Electrochimica Acta*, vol. 125, pp. 586–592, 2014.

[2] S. Mekhilef, R. Saidur, and A. Safari, "A review on solar energy use in industries," *Renewable and Sustainable Energy Reviews*, vol. 15, no. 4, pp. 1777–1790, 2011.

[3] D. Y. C. Leung and Y. Yang, "Wind energy development and its environmental impact: a review," *Renewable and Sustainable Energy Reviews*, vol. 16, no. 1, pp. 1031–1039, 2012.

[4] N. Khan, A. Kalair, N. Abas, and A. Haider, "Review of ocean tidal, wave and thermal energy technologies," *Renewable and Sustainable Energy Reviews*, vol. 72, pp. 590–604, 2017.

[5] I. U. Khan, M. H. Othman, H. Hashim et al., "Biogas as a renewable energy fuel – a review of biogas upgrading, utilisation and storage," *Energy Conversion and Management*, vol. 150, pp. 277–294, 2017.

[6] J. Liu, J. Wang, C. Xu et al., "Advanced energy storage devices: basic principles, analytical methods, and rational materials design," *Advanced Science*, vol. 5, no. 1, article 1700322, 2018.

[7] P. Simon and Y. Gogotsi, "Materials for electrochemical capacitors," *Nature Materials*, vol. 7, no. 11, pp. 845–854, 2008.

[8] J. R. Miller and P. Simon, "Electrochemical capacitors for energy management," *Science*, vol. 321, no. 2008, pp. 651-652, 2008.

[9] M. Conte, "Supercapacitors technical requirements for new applications," *Fuel Cells*, vol. 10, no. 5, pp. 806–818, 2010.

[10] X. Qi, W. Zheng, X. Li, and G. He, "Multishelled NiO Hollow Microspheres for High-performance Supercapacitors with Ultrahigh Energy Density and Robust Cycle Life," *Scientific Reports*, vol. 6, pp. 1–10, 2016.

[11] Q. Zhu, D. Zhao, M. Cheng et al., "A new view of supercapacitors: integrated supercapacitors," *Advanced Energy Materials*, vol. 9, no. 36, article 1901081, 2019.

[12] A. L. Brisse, P. Stevens, G. Toussaint, O. Crosnier, and T. Brousse, "$Ni(OH)_2$ and NiO Based Composites: Battery Type Electrode Materials for Hybrid Supercapacitor Devices," *Materials*, vol. 11, no. 7, p. 1178, 2018.

[13] B. E. Conway, "Transition from 'supercapacitor' to 'battery' behavior in electrochemical energy storage," in *Proceedings of the 34th International Power Sources Symposium*, pp. 319–327, Cherry Hill, NJ, USA, 1990.

[14] R. Kötz and M. Carlen, "Principles and applications of electrochemical capacitors," *Electrochimica Acta*, vol. 45, no. 15-16, pp. 2483–2498, 2000.

[15] S. Sahoo, R. Mondal, D. J. Late, and C. S. Rout, "Electrodeposited nickel cobalt manganese based mixed sulfide nanosheets for high performance supercapacitor application," *Microporous and Mesoporous Materials*, vol. 244, pp. 101–108, 2017.

[16] L. Zhang and X. S. Zhao, "Carbon-based materials as supercapacitor electrodes," *Chemical Society Reviews*, vol. 38, no. 9, pp. 2520–2531, 2009.

[17] S. Li, R. Feng, M. Li et al., "Needle-like CoO nanowire composites with NiO nanosheets on carbon cloth for hybrid flexible supercapacitors and overall water splitting electrodes," *RSC Advances*, vol. 10, no. 61, pp. 37489–37499, 2020.

[18] Y. Zhang, H. Hu, Z. Wang et al., "Boosting the performance of hybrid supercapacitors through redox electrolyte-mediated capacity balancing," *Nano Energy*, vol. 68, article 104226, 2020.

[19] H. Wang, H. Yi, X. Chen, and X. Wang, "Facile synthesis of a nano-structured nickel oxide electrode with outstanding pseudocapacitive properties," *Electrochimica Acta*, vol. 105, pp. 353–361, 2013.

[20] G. Murugadoss, J. Ma, X. Ning, and M. R. Kumar, "Selective metal ions doped CeO_2 nanoparticles for excellent photocatalytic activity under sun light and supercapacitor application," *Inorganic Chemistry Communications*, vol. 109, article 107577, 2019.

[21] A. A. Yadav, Y. M. Hunge, and S. B. Kulkarni, "Synthesis of multifunctional $FeCo_2O_4$ electrode using ultrasonic treatment for photocatalysis and energy storage applications," *Ultrasonics Sonochemistry*, vol. 58, article 104663, 2019.

[22] P. Zhao, M. Yao, H. Ren, N. Wang, and S. Komarneni, "Nanocomposites of hierarchical ultrathin MnO_2 nanosheets/hollow carbon nanofibers for high-performance asymmetric supercapacitors," *Applied Surface Science*, vol. 463, pp. 931–938, 2019.

[23] R. Kumar, A. Agrawal, T. Bhuvana, and A. Sharma, "Porous indium oxide hollow spheres (PIOHS) for asymmetric electrochemical supercapacitor with excellent cycling stability," *Electrochimica Acta*, vol. 270, pp. 87–95, 2018.

[24] A. Zhang, W. Zheng, Z. Yuan et al., "Hierarchical NiMn-layered double hydroxides@CuO core-shell heterostructure in-situ generated on $Cu(OH)_2$ nanorod arrays for high performance supercapacitors," *Chemical Engineering Journal*, vol. 380, article 122486, 2020.

[25] F. Naeem, S. Naeem, Z. Zhao et al., "Atomic layer deposition synthesized ZnO nanomembranes: a facile route towards stable supercapacitor electrode for high capacitance," *Journal of Power Sources*, vol. 451, article 227740, 2020.

[26] W. Huang, L. Li, D. Liang et al., "In situsynthesis of a 3D highly porous NiO film electrode with enhanced performance for supercapacitors," *Inorganic Chemistry Frontiers*, vol. 6, no. 10, pp. 2927–2934, 2019.

[27] S. Zhang, Y. Pang, Y. Wang et al., "NiO nanosheets anchored on honeycomb porous carbon derived from wheat husk for symmetric supercapacitor with high performance," *Journal of Alloys and Compounds*, vol. 735, pp. 1722–1729, 2018.

[28] W. Zuo, C. Xie, P. Xu, Y. Li, and J. Liu, "A novel phase-transformation activation process toward Ni-Mn-O nanoprism arrays for 2.4 V ultrahigh-voltage aqueous supercapacitors," *Advanced Materials*, vol. 29, no. 36, article 1703463, 2017.

[29] Y. Bi, A. Nautiyal, H. Zhang, J. Luo, and X. Zhang, "One-pot microwave synthesis of NiO/MnO_2 composite as a high-performance electrode material for supercapacitors," *Electrochimica Acta*, vol. 260, pp. 952–958, 2018.

[30] V. D. Silva, T. A. Simões, F. J. A. Loureiro et al., "Solution blow spun nickel oxide/carbon nanocomposite hollow fibres as an efficient oxygen evolution reaction electrocatalyst," *International Journal of Hydrogen Energy*, vol. 44, no. 29, pp. 14877–14888, 2019.

[31] G. Manibalan, G. Murugadoss, P. Kuppusami, N. Kandhasamy, and M. Rajesh Kumar, "Synthesis of heterogeneous NiO nanoparticles for high-performance electrochemical supercapacitor application," *Journal of Materials Science: Materials in Electronics*, vol. 32, no. 5, pp. 5945–5954, 2021.

[32] L. Wang, H. Tian, D. Wang, X. Qin, and G. Shao, "Preparation and electrochemical characteristic of porous NiO supported by sulfonated graphene for supercapacitors," *Electrochimica Acta*, vol. 151, pp. 407–414, 2015.

[33] M. B. Poudel, A. A. Kim, P. C. Lohani, D. J. Yoo, and H. J. Kim, "Assembling zinc cobalt hydroxide/ternary sulfides heterostructure and iron oxide nanorods on three-dimensional hollow porous carbon nanofiber as high energy density hybrid supercapacitor," *Journal of Energy Storage*, vol. 60, article 106713, 2023.

[34] M. B. Poudel and H. J. Kim, "Synthesis of high-performance nickel hydroxide nanosheets/gadolinium doped-α-MnO_2 composite nanorods as cathode and Fe_3O_4/GO nanospheres as anode for an all-solid-state asymmetric supercapacitor," *Journal of Energy Chemistry*, vol. 64, pp. 475–484, 2022.

[35] S. D. Dhas, P. S. Maldar, M. D. Patil et al., "Synthesis of NiO nanoparticles for supercapacitor application as an efficient electrode material," *Vacuum*, vol. 181, article 109646, 2020.

[36] M. Sethi, U. S. Shenoy, and D. K. Bhat, "Hassle-free solvothermal synthesis of NiO nanoflakes for supercapacitor application," *Physica B: Condensed Matter*, vol. 611, article 412959, 2021.

[37] M. Jayachandran, A. Rose, T. Maiyalagan, N. Poongodi, and T. Vijayakumar, "Effect of various aqueous electrolytes on the electrochemical performance of α-MnO_2 nanorods as electrode materials for supercapacitor application," *Electrochimica Acta*, vol. 366, article 137412, 2021.

[38] X. H. Xia, J. P. Tu, Y. Q. Zhang et al., "Three-dimentional porous nano-Ni/$Co(OH)_2$ nanoflake composite film: a pseudocapacitive material with superior performance," *Journal of Physical Chemistry C*, vol. 115, no. 45, pp. 22662–22668, 2011.

[39] Q. Lu, *Supercapacitor Electrodes with High-energy and power densities prepared from monolithic NiO/Ni Nanocomposite*, American Physical Society, 2012.

[40] J. S. Gao, T. Lian, Z. Liu, and Y. He, "Efficient NiO/RGO combination for high-cycling-stability supercapacitors by an alkaline hydrothermal strategy," *Journal of Applied Electrochemistry*, vol. 52, no. 7, pp. 1045–1052, 2022.

[41] A. Vazhayil, J. Thomas, and N. Thomas, "Enhanced electrochemical performance of facilely synthesized cobalt doped cubic NiO nanoflakes for supercapacitor application," *Journal of Energy Storage*, vol. 55, article 105498, 2022.

[42] N. Jayababu, S. Jo, Y. Kim, and D. Kim, "Preparation of NiO decorated CNT/ZnO core-shell hybrid nanocomposites with the aid of ultrasonication for enhancing the performance of hybrid supercapacitors," *Ultrasonics Sonochemistry*, vol. 71, article 105374, 2021.

[43] A. Khan, M. Shkir, S. A. Ansari et al., "One-pot flash combustion synthesis of Fe@NiO nanocomposites for supercapacitor applications," *Ceramics International*, vol. 47, no. 7, pp. 9024–9033, 2021.

[44] S. H. S. Pai, A. Sasmal, A. K. Nayak, and H. Han, "Facile Solvothermal Synthesis of NiO/g-C3n4 Nanocomposite for Enhanced Supercapacitor Application," *SSRN*, p. 23, 2023.

[45] S. Verma and R. K. Dutta, "Sunlight assisted photocatalytic removal of trypan blue dye using g-carbon nitrides sheets as sunlight-active photocatalyst," *Nanotechnology for Environmental Engineering*, vol. 7, no. 1, pp. 67–74, 2022.

[46] W. S. Chen, S. H. Yang, W. C. Tseng, W. W. S. Chen, and Y. C. Lu, "Utilization of nanoporous nickel oxide as the hole injection layer for quantum dot light-emitting diodes," *ACS Omega*, vol. 6, no. 20, pp. 13447–13455, 2021.

[47] M. F. Al-Kuhaili, S. H. A. Ahmad, S. M. A. Durrani, M. M. Faiz, and A. Ul-Hamid, "Application of nickel oxide thin films in NiO/Ag multilayer energy-efficient coatings," *Materials Science in Semiconductor Processing*, vol. 39, pp. 84–89, 2015.

[48] J. T. Titantah and D. Lamoen, "Carbon and nitrogen 1s energy levels in amorphous carbon nitride systems: XPS interpretation using first-principles," *Diamond and Related Materials*, vol. 16, no. 3, pp. 581–588, 2007.

[49] J. Zemek, J. Zalman, and A. Luches, "XAES and XPS study of amorphous carbon nitride layers," *Applied Surface Science*, vol. 133, no. 1-2, pp. 27–32, 1998.

[50] M. A. Peck and M. A. Langell, "Comparison of nanoscaled and bulk NiO structural and environmental characteristics by XRD, XAFS, and XPS," *Chemistry of Materials*, vol. 24, no. 23, pp. 4483–4490, 2012.

[51] T. Huang, W. Zhang, S. Pan et al., "General synthesis strategy for hollow porous prismatic graphitic carbon nitride: a high-performance photocatalyst for H_2 production and degradation of RhB," *Journal of Materials Science*, vol. 55, no. 14, pp. 6037–6050, 2020.

[52] X. Zheng, Y. Sun, H. Qin, and Z. Ji, "Solar-charged pseudocapacitors: simultaneous conversion and storage of solar energy in ZnO@NiO nanorod arrays," *Journal of Alloys and Compounds*, vol. 781, pp. 351–356, 2019.

[53] Y. Ghalmi, F. Habelhames, A. Sayah et al., "Enhancement of the capacitance properties and the photoelectrochemical performances of P_3HT film by incorporation of nickel oxide nanoparticles," *Ionics*, vol. 25, no. 6, pp. 2903–2912, 2019.

[54] X. Li, J. Li, Y. Zhang, and P. Zhao, "Synthesis of Ni-MOF derived NiO/rGO composites as novel electrode materials for high performance supercapacitors," *Colloids and Surfaces A: Physicochemical and Engineering Aspects*, vol. 622, article 126653, 2021.

[55] X. Y. Hou, X. L. Yan, X. Wang, and Q. G. Zhai, "Tuning the porosity of mesoporous NiO through calcining isostructural Ni-MOFs toward supercapacitor applications," *Journal of Solid State Chemistry*, vol. 263, pp. 72–78, 2018.

[56] V. Sannasi, M. Maheswari, K. Ramachandran, and S. Karuppuchamy, "Microwave synthesis of Sn-doped NiO/CNT composites: the effect of Sn incorporation on their supercapacitive properties," *Journal of Electronic Materials*, vol. 50, no. 11, pp. 6102–6113, 2021.

[57] B. Pal, S. Yang, S. Ramesh, V. Thangadurai, and R. Jose, "Electrolyte selection for supercapacitive devices: a critical review," *Nanoscale Advances*, vol. 1, no. 10, pp. 3807–3835, 2019.

[58] A. M. Teli, S. A. Beknalkar, S. M. Mane et al., "Facile hydrothermal deposition of copper-nickel sulfide nanostructures on nickel foam for enhanced electrochemical performance and kinetics of charge storage," *Applied Surface Science*, vol. 571, article 151336, 2022.

[59] S. Rudra, N. Deka, A. K. Nayak, M. Pradhan, and G. K. Dutta, "Facile hydrothermal synthesis of Au-Mn_3O_4 decorated graphene oxide nanocomposites for solid-state supercapacitor," *Journal of Energy Storage*, vol. 50, article 104615, 2022.

[60] A. K. Nayak and T. Gopalakrishnan, "Phase- and crystal structure-controlled synthesis of Bi_2O_3, Fe_2O_3, and $BiFeO_3$ nanomaterials for energy storage devices," *ACS Applied Nano Materials*, vol. 5, no. 10, pp. 14663–14676, 2022.

[61] M. Jalalah, S. S. Sivasubramaniam, B. Aljafari et al., "Biowaste assisted preparation of self-nitrogen-doped nanoflakes carbon framework for highly efficient solid-state supercapacitor application," *Journal of Energy Storage*, vol. 54, article 105210, 2022.

[62] T. Brezesinski, J. Wang, S. H. Tolbert, and B. Dunn, "Ordered mesoporous α-MoO_3 with iso-oriented nanocrystalline walls for thin-film pseudocapacitors," *Nature Materials*, vol. 9, no. 2, pp. 146–151, 2010.

[63] C. L. Pearline, M. J. Abel, A. Pramothkumar, N. Senthilkumar, P. Anbalagan, and J. J. Prince, "Investigation on structural, optical and electrochemical behavior of NiO/$ZnMn_2O_4$ ternary nanocomposites via two-step synthesis approach for supercapacitor application," *Chemical Papers*, vol. 75, no. 2, pp. 641–651, 2021.

[64] V. Balasubramani, S. Chandraleka, T. S. Rao, R. Sasikumar, M. R. Kuppusamy, and T. M. Sridhar, "Review—recent advances in electrochemical impedance spectroscopy based toxic gas sensors using semiconducting metal oxides," *Journal of the Electrochemical Society*, vol. 167, no. 3, article 037572, 2020.

[65] J. Mohanta, U. P. Singh, S. K. Panda, and S. Si, "Enhancement of Li^+ ion conductivity in solid polymer electrolytes using surface tailored porous silica nanofillers," *Advances in Natural Sciences: Nanoscience and Nanotechnology*, vol. 7, article 035011, 2016.

[66] A. L. Yan, W. D. Wang, B. Q. Wang, X. C. Wang, and J. P. Cheng, "Core-shell structured Co_3O_4@$NiCo_2O_4$ nanowires on nickel foam for supercapacitors," *Journal of Electroanalytical Chemistry*, vol. 907, article 116061, 2022.

[67] K. Sun, J. Li, H. Peng, E. Feng, G. Ma, and Z. Lei, "Promising nitrogen-doped porous nanosheets carbon derived from pomegranate husk as advanced electrode materials for supercapacitors," *Ionics*, vol. 23, no. 4, pp. 985–996, 2017.

[68] Q. Wang, J. Yan, Y. Wang et al., "Three-dimensional flower-like and hierarchical porous carbon materials as high-rate performance electrodes for supercapacitors," *Carbon*, vol. 67, pp. 119–127, 2014.

[69] G. Ghanashyam and H. K. Jeong, "Plasma treated carbon nanofiber for flexible supercapacitors," *Journal of Energy Storage*, vol. 40, article 102806, 2021.